Journal of Materials Chemistry A

Separator-Free and Concentrated LiNO3 Electrolyte Cells Enable Uniform Lithium Electrodeposition

Journal:	*Journal of Materials Chemistry A*
Manuscript ID	TA-ART-10-2019-010929.R1
Article Type:	Paper
Date Submitted by the Author:	10-Dec-2019
Complete List of Authors:	Rodriguez, Rodrigo; University of Texas at Austin, Department of Chemical Engineering Edison, Ruth; University of Texas at Austin, Department of Chemical Engineering Stephens, Ryan; Shell Sun, Ho-Hyun; University of Texas at Austin, Department of Chemical Engineering Heller, A; The University of Texas at, McKetta Dept of Chemical Engineering Mullins, Charles; University of Texas at Austin, Department of Chemical Engineering

Separator-Free and Concentrated $LiNO_3$ Electrolyte Cells Enable Uniform Lithium Electrodeposition

Rodrigo Rodriguez[†], Ruth A. Edison[¥], Ryan M. Stephens[⊥], Ho-Hyun Sun[†], Adam Heller[†∥], and C. Buddie Mullins[†‡§∥]*

[†]McKetta Department of Chemical Engineering, The University of Texas at Austin, Austin, Texas 78712-1589, United States

[¥]Department of Physics, The University of Texas at Austin, Austin, Texas 78712-1192, United States

[‡]Texas Materials Institute, The University of Texas at Austin, Austin, Texas 78712-1591, United States

[§]Department of Chemistry, The University of Texas at Austin, Austin, Texas 78712-1224, United States

[∥]Center for Electrochemistry, The University of Texas at Austin, Austin Texas 78712-0165, United States

[⊥]Shell International Exploration & Production Inc., Houston, Texas 77082, United States

*E-mail: mullins@che.utexas.edu.

Imaging of lithium electrodepositions revealed that in the absence of a compressed porous separator, achieved via a plastic washer, dendrite-free lithium was deposited from glyme solutions of 1M $LiNO_3$. When the 1M $LiNO_3$ in glyme was coupled with a 1M LiFSI salt, high coulombic efficiencies were also attainable in both Li|Cu and anode-free LFP|Cu cells. However, dendrite resurgence was observed in cycled lithium coin cell electrodes when a porous separator was utilized. This was attributed to the restriction of Li^+ flux to the electrode surface induced by the porous and tortuous structure of the polymer separator. At these pores, localized current densities, which exceeded the applied current density, and a non-uniform Li^+ flux resulted in dendritic lithium growth. Replacement of the separator by a washer normalized the current distribution and provided for non-dendritic lithium deposits in coin cells.

The successful implementation of metallic lithium anodes would greatly enhance the energy density of current lithium-ion batteries (LIBs). It is estimated that lithium's ultra-high gravimetric capacity (3860 mAh g^{-1}), coupled with current metal oxide cathode materials, could increase the gravimetric energy densities of LIBs by approximately 35%.[1] However, the well-known problem of lithium's poor plating/stripping efficiency and dendrite formation has stalled its commercialization.[2–4] Thus solvent and salt compositions must be meticulously selected so that an optimal solid electrolyte interphase (SEI) is formed capable of mitigating dendrite formation and maintaining a high cycling efficiency.[3,5–9] This SEI would ideally have a uniform thickness, high lithium-ion flux permeability, and be chemically and mechanically stable.[10,11]

Owing to their cost and simplicity, coin cells are the most common battery form factor used in academic research. Thus, the majority of the reported lithium deposition morphologies in literature come from coin cell electrodes cycled with porous polymer separators. When a polymer separator is compressed in the closure of a coin cell, the pore volume can decrease by over 50% causing a considerable loss to lithium-ion transport.[12] A reduction in lithiu-ion flux to the electrode surface increases the concentration polarization in a cell that further promotes the formation of

dendrites.[13] Dendrite formation is also exacerbated by the inhomogeneous lithium-ion flux to electrode surfaces caused by constricting lithium-ion flow to the locations where the pores meet the electrode.[14–16] Additionally increasing, the magnitude of the cell stack pressure exerted on the deposited electrode can also play a major role in the lithium turnover and porosity by forming a denser deposition layer.[2,3,17,18] The Dahn group recently reported that anode-free pouch cell electrodes can also benefit from compressive forces, with some electrolyte compositions benefitting from the electrode stack pressure more than others.[19,20] Applying a constant, homogenous pressure on the lithium electrode surface inside a coin cell is simple, however applying a uniform stack pressure on the much larger electrodes used in pouch cells would not be practical.[21]

Recently, our group conducted a study on the lithium deposition morphology of a number of ether and carbonate-based electrolytes in a home-built visualization cell, which operated without a compressed separator.[5] This visualization cell allowed us to observe electrodeposits of lithium in carbonate, fluorine donating (such as fluoroethylene carbonate/$LiPF_6$),[22,23] and highly concentrated lithium bis(fluorosulfonyl)imide (LiFSI) electrolytes.[24] Many of the electrolytes in our study had been previously reported to have dendrite-free morphology, a claim that was supported by ex situ SEM imaging of lithium electrodes retrieved from coin cells. However, we found that the majority of lithium deposits displayed similar dendritic formations despite having large differences in coin cell cycling efficiencies.[5] Out of all the electrolytes sampled, only the highly concentrated 3M $LiNO_3$ electrolyte reported by Zhang et al.[25] demonstrated complete dendrite inhibition without the aid of cell stack pressure in the visualization cell. However, the

capacity retention of this electrolyte was poorly retained in anode-free lithium iron phosphate (LFP)|Cu cells.[5]

$LiNO_3$ is a common additive in ether-based electrolytes because it can react with lithium to form passivating $LiNO_x$ and Li_2O moieties in the SEI.[25–27] SEIs enriched with these $LiNO_3$ decomposition products are more electrochemically stable and lithium-ion permeable which enable lithium anodes to cycle at high efficiencies with improved deposition morphologies.[7,25,28] Even when $LiNO_3$ is present in additive amounts as small as 1 wt%, lithium nuclei morphology is dramatically altered from the typical needle-like to spherical electrodeposits.[4,29] However, the initially compact spherical deposition morphology is transient; optical imaging shows that dendrites reemerge as more charge is passed.[5,30,31]

In this communication, we show that complete dendrite mitigation with high cycling efficiencies is achievable through the use of an electrolyte consisting of 1M $LiNO_3$ with 1M LiFSI in dimethoxyethane (DME). The 4M LiFSI in DME electrolyte proposed by Zhang et al. was chosen as a basis for comparison to the $LiNO_3$-based electrolytes in this work since this electrolyte has been shown to yield compact lithium electrodeposits in coin cells with high cycling efficiencies.[24] Optical imaging from a dedicated visualization cell revealed that a 1M concentration of $LiNO_3$ was sufficient to mitigate dendrite formation in the absence of a porous separator. Though electrolytes utilizing DME demonstrated the best capacity retention in the anode-free cells, these electrolytes could not be cycled at current densities higher than 0.5 mA cm^{-2} in Li|Cu cells. By utilizing diethylene glycol dimethyl ether (DGDE) as a cosolvent with DME, 1:1 vol%, the Li|Cu coin cells could be cycled up to 1 mA cm^{-2} while retaining high coulombic efficiencies. In contrast to the dendrite free depositions seen in the visualization cell, imaging from electrodes

cycled in symmetrical Li|Li coin cells revealed that depositions in the concentrated $LiNO_3$ electrolytes resulted in three-dimensional structures when a polymer separator was utilized. However, uniform lithium electrodeposits were attainable when the separator was replaced with a plastic washer whose void volume was filled with electrolyte. Evidently, constricting the lithium-ion flux, and therefore the deposition of metallic lithium, to the points of contact between the separator pores and the electrode was responsible for this discrepancy. At these points, the localized current density exceeded the galvanostatically applied current density. In contrast, the applied current density was uniform throughout the entire electrode when a washer was utilized which restored the uniform deposition morphology. Finally, time-of-flight secondary ion mass spectrometry (ToF-SIMS) was employed to compare the SEIs formed on lithium electrodes as a function of electrolyte composition.

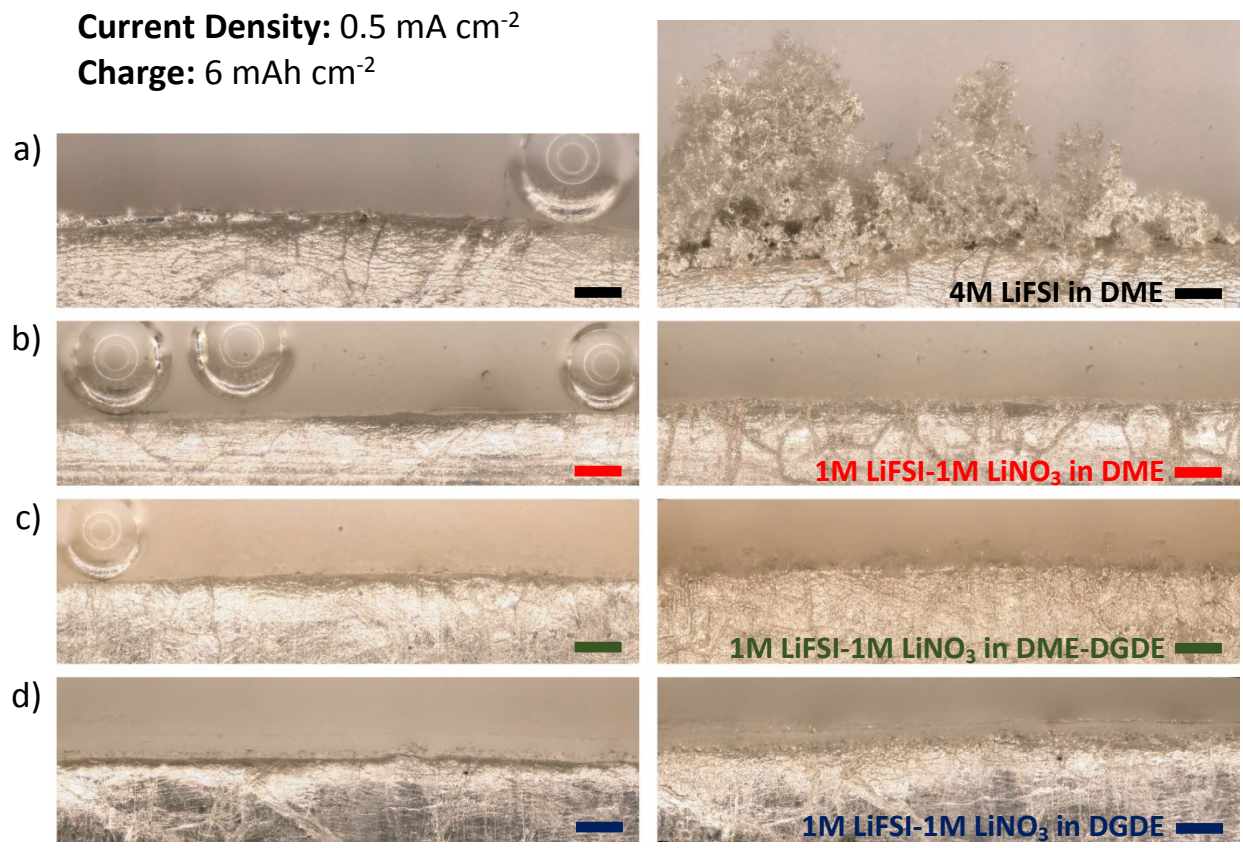

Figure 1. Lithium electrodes before (left) and after (right) passing 6 mAh cm^{-2} of charge with a current density of 0.5 mA cm^{-2}. Electrolytes utilized: (a) 4M LiFSI in DME, (b) 1M LiFSI with 1M $LiNO_3$ in DME, (c) 1M LiFSI with 1M $LiNO_3$ in DME and DGDE (1:1

Figure 1 shows high-resolution optical imaging of depositions onto lithium electrodes in various electrolytic solutions before and after 6 mAh cm^{-2} of charge was passed at 0.5 mA cm^{-2}; this large quantity of charge was chosen to highlight the dendrite inhibition capabilities of the $LiNO_3$ electrolytes. A schematic illustrating the optical cell design used to image these electrodes is shown in **Figure S1**. The cells were constructed with two lithium electrodes, flooded with electrolyte, and hermetically sealed in a glovebox with no separator. **Figure 1a** shows that the 4M LiFSI in DME electrolyte formed the typical high-surface area, protruding lithium electrodeposits. This deposition morphology is unfavorable as it introduces highly reactive, pristine lithium metal

to the electrolyte; these protruding structures are also prone to electrically disconnect from the lithium surface and have the potential to cause cell shorting.[3,4] The rest of the images in **Figure 1** show the positive effect of the addition of 1M $LiNO_3$ to electrolyte compositions in suppressing the formation of branched structures. **Figure S2** shows that this deposition morphology was also reproducible at faster charge rates. **Figure S3** shows that dendrite formation diminishes in electrolytes consisting of 1M LiFSI in DME as the $LiNO_3$ concentration is increased from 0 to 1M.

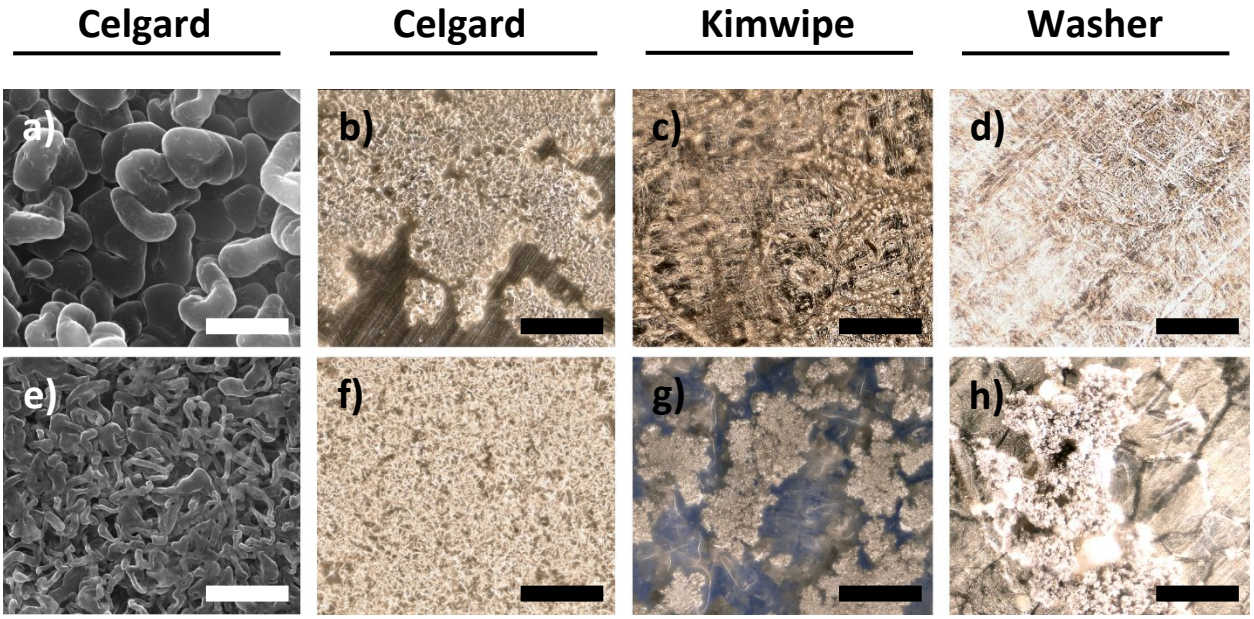

Figure 2. SEM images (a, e) and optical images (b, c, d, f, g, h) of 1 mAh cm^{-2} Li-deposits cycled at 1.0 mA cm^{-2}. Top (a – d): 1M LiFSI with 1M $LiNO_3$ in DGDE; bottom (e – h): 4M LiFSI in DME. Depositions on Li utilizing small pore Celgard separators (a, b, e, f), large pore Kimwipe separator (c), and washer (d, h) are shown. g) shows

Figure 2 compares the electrodeposits of lithium in the 1M LiFSI with 1M $LiNO_3$ in DGDE (top row, a – d) and the 4M LiFSI in DME electrolyte (bottom row, e – h) retrieved from symmetrical Li|Li cells. The SEM and optical imaging in **Figure 2a** and **b** revealed that the 1M

$LiNO_3$ electrolyte electrodeposited thick, three-dimensional structures in coin cells utilizing the porous polymer separator. Though this deposition morphology is attractive for producing dense electrodeposits with reduced surface area, it appeared to contradict the results of the optical imaging where no such structures were observed. In order to replicate the electrodeposition conditions of the visualization cell on the lithium disk electrodes, a high-density polyethylene washer was inserted into the coin cells in place of the Celgard separator. The void volume of the washer was filled with electrolyte, and the cells were cycled. **Figure 2d** shows that the uncompressed and separator-free depositions in the concentrated $LiNO_3$ electrolyte were able to attain uniform lithium morphology confirming the results of the visualization cell; SEM imaging of the lithium morphology attained with washer depositions is shown in **Figure S4**. In order to verify that the difference in volume of electrolyte of the polymer versus the washer was not responsible for the difference in the deposition morphology observed, a washer and polymer separator were used together; however, lithium depositions with the polymer separator and washer also showed a reemergence of three-dimensional structures (**Figure S5**). Deposition morphologies similar to those attained using the $LiNO_3$ electrolyte were also observed when the 4M LiFSI electrolyte was utilized in coin cells containing the polymer separator (**Figure 2e**). However, replacing the separator with a plastic washer did not smooth lithium deposits in this 4M LiFSI in DME electrolyte (**Figure 2h**). Uninhibited by the coin cell stack pressure, the 4M LiFSI in DME electrodeposits formed dendritic lithium.

In order to study the role of the pore size on the deposition morphology, the small pore Celgard separator was replaced with an 80 μm thick, fibrous Kimwipe separator possessing large, straight-through channels (**Figure S6**). These large channels allowed us to reduce the true current

density where the pores contacted the electrode surface. Coin cells utilizing only the Kimwipe separator and the concentrated $LiNO_3$ electrolyte were able to cycle without shorting. Their lithium deposition morphology was globular (**Figure 2c**), distinctly different from those of the Celgard separator cells. On the other hand, the cells with Kimwipe separators utilizing the 4M LiFSI in DME electrolyte shorted promptly when charged. Imaging of the fibrous separator with dendrites protruding through it is shown in **Figure 2g** (the lithium electrode is not shown since the deposits were removed when the fibrous separator was lifted off of the electrode surface). The results of **Figure 2** are summarized in the illustration shown in **Figure 3**.

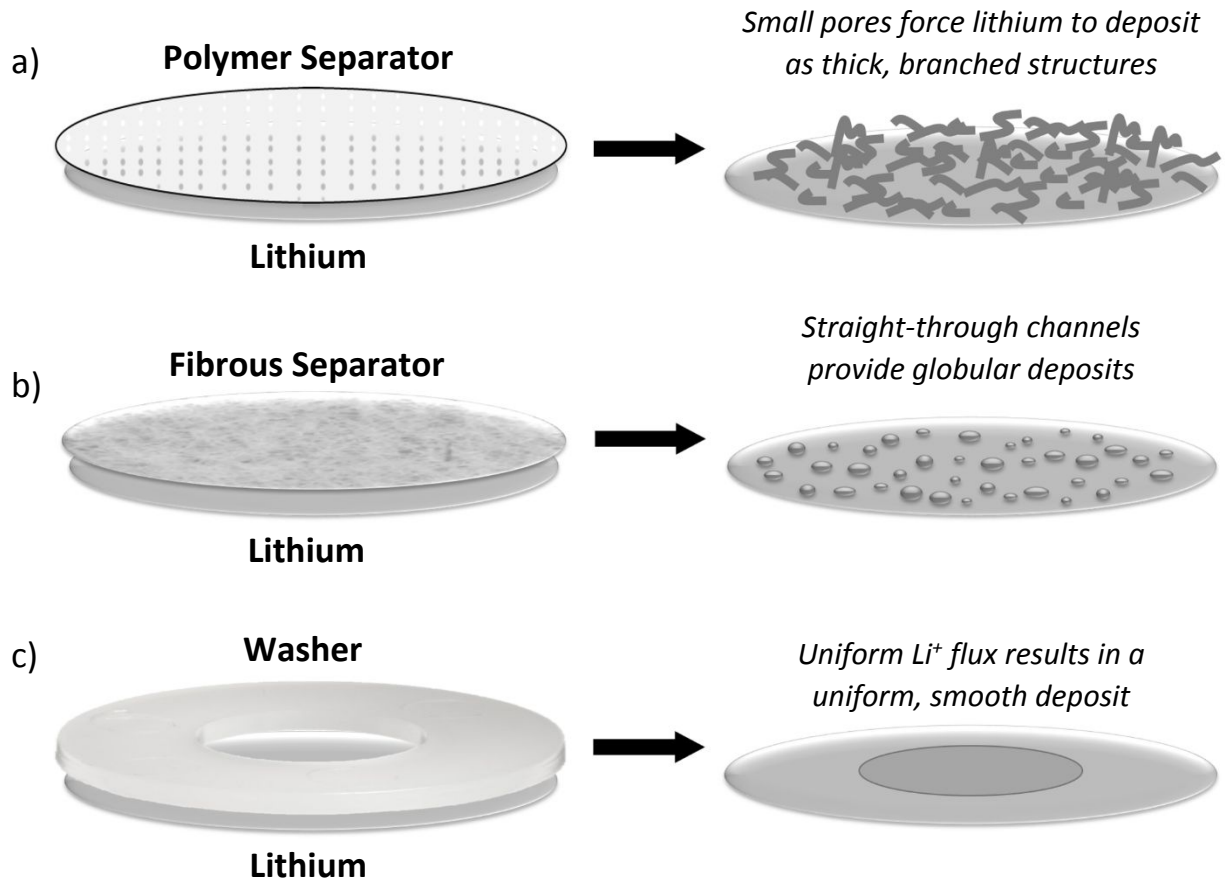

Figure 3. Schematic illustrating the deposition morphology of lithium when a concentrated $LiNO_3$ electrolyte is utilized in cells containing small contacting pores (a),

Peng Bai et al recently demonstrated that after a certain lithium plating capacity, defined as Sand's capacity, a transition in deposition morphology from mossy deposits to dendritic ones occurs.[13] This change in growth mechanism was caused by a depletion of lithium ions near the deposited lithium electrode which was shown to produce diffusion-limited, dendritic deposits. By constructing symmetrical lithium cells in which a nanoporous ceramic separator was sandwiched between two washers, Bai identified three lithium deposition growth modes, defined by the applied current density, which could lead to whisker, moss, or dendritic deposits.[32] In our lithium depositions in coin cells utilizing washers (**Figure 2d**), whisker, mossy, and dendritic growths were absent when the concentrated $LiNO_3$ electrolyte was utilized. If whisker and mossy lithium growth is a product of SEI breakage or incomplete SEI formation as Bai has suggested, then the concentrated $LiNO_3$ electrolyte must form an SEI that can withstand breakage as the lithium is deposited such that a uniform lithium morphology is realized and maintained in the visualization cell.

Reemergence of protruding, high-surface area lithium deposits observed on lithium electrodes cycled in coin cells (**Figure 2 a,b**) was not attributed to a depletion of lithium ions at the deposited surface.[13,33,34] The thick dendrites produced by the $LiNO_3$ electrolyte in **Figure 2a** are characteristic of the whisker growth mode (root growth), not a dendritic growth mode (tip growth).[32] Additionally, only a moderate amount of lithium (1 mAh cm^{-2}) at a slow charge rate (1 mA cm^{-2}) was deposited which should result in a deposition regime far below the Sand's capacity. Rather, it was the localization of the lithium-ion flux caused by pressing a porous polymer separator on to the lithium surface that resulted in the reemergence of high-surface area deposits in the coin cells electrodes. This can also be seen in the work of Han et al, where growth of copper

through a nanoporous media can change depending on the current density and the surface charge present.[35,36] These results are also consistent with the work reported by the Zhang group. They found that employing a solid-state fast ionic conductor on the polymer separator surface facing a lithium electrode produced a smoother electrodeposition layer via a redistribution of the ionic flux to the deposited lithium surface.[14]

Consequently, it appears that both the electrode stack pressure and the Celgard separator have a profound effect on the formation of dendritic structures. Increasing compression in cells is known to have a positive impact on the lithium cycling efficiency.[17,37] This is due to the fact that lithium dendrites form a dense deposition layer under compression leading to greater electrical contact throughout the deposit, which decreases the formation of dead lithium.[3,21] However, our results show that the application of cell stack pressure may not be universally required for improving the density of the lithium electrodeposition layer.

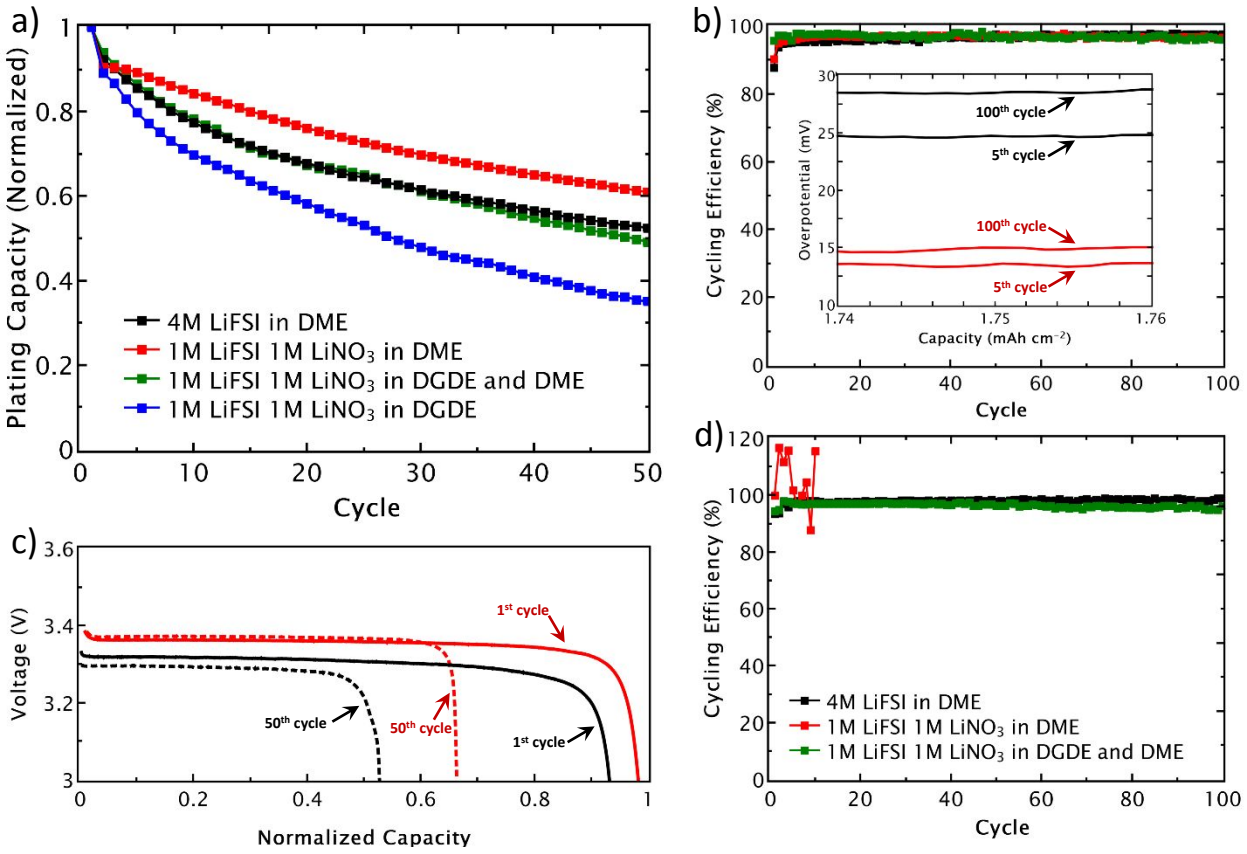

Figure 4. (a) Retention of the coulombic capacity of LFP|Cu cells for different electrolytic solutions normalized to the first cycle. (b) Cycling efficiencies of Li|Cu cells cycled at 0.5 mA cm^{-2} for 2.5 mAh cm^{-2}. Inset in b) demonstrates the stripping overpotential curves for the Li|Cu cells cycled at 0.5 mA cm^{-2} for the 5^{th} and 100^{th}

Figure 4 shows the cycling performance of lithium coin cells utilizing only the porous polymer separators. **Figure 4a** shows the capacity retention of the plated lithium normalized to the first deposition cycle in the anode-free LFP|Cu cells. All cells were cycled at 0.2 mA cm^{-2} and had approximately 1.7 mAh cm^{-2} of lithium charge stored in the LFP electrodes. The anode-free coin cell testing revealed that the 1M LiFSI and 1M $LiNO_3$ with the DME solvent was the best performing electrolyte. When the solvent was replaced with DGDE, the capacity retention was markedly lower. This reduced capacity retention can be attributed to the decreasing stability of

glyme solvents towards lithium metal as chain length is increased.[8] Electrochemical impedance spectra of symmetrical Li|Li cells in **Figure S7** also revealed that the cell impedance was lower for the DME solvent electrolyte than the DGDE solvent. When the DME and DGDE solvents were combined in a 1:1 ratio (vol%), capacity retention rivaling the 4M LiFSI in DME electrolyte was obtained (**Figure 4a**). Additional LFP|Cu cell capacity retention curves utilizing varying $LiNO_3$, LiFSI, and lithium bis(trifluoromethanesulfonyl)imide (LiTFSI) salt concentrations are shown in **Figure S8**. **Figure 4c** shows the lithium stripping voltage curves for the LFP|Cu cells in **Figure 4a**. After 50 cycles and approximately 34% loss in cyclable lithium, a 10 mV drop in the stripping voltage is observed for the $LiNO_3$ electrolyte. On the other hand, the 4M LiFSI in DME electrolyte had a voltage drop of 26 mV after losing around 48% of the total cyclable lithium on the 50^{th} cycle.

Coulombic efficiency tests of Li|Cu cells with excess, thick lithium anodes are also shown in **Figure 4**. At a charge rate of 0.5 mA cm^{-2} (**Figure 4b**), coulombic efficiencies ranging from 96 – 98% were attainable for all electrolytes when passing 2.5 mAh cm^{-2} of charge. The inset in **Figure 4b** shows the stripping curves for the overpotentials of the Li|Cu cells. The color of the overpotential curves match the coulombic efficiency curves shown in the legend. The stripping overpotential curves shown in **Figure 4b** revealed that a lower overpotential was required to pass a constant current in the 1M $LiNO_3$ with 1M LiFSI in DME electrolyte than the 4M LiFSI in DME electrolyte. Additionally, the difference in the baseline stripping overpotentials between the 5^{th} and 100^{th} cycles were also lower in the $LiNO_3$ electrolyte. Li|Cu cells cycled at 1.0 mA cm^{-2} are shown in **Figure 4d**. At this current density, the 1M LiFSI with 1M $LiNO_3$ in DME electrolyte would result in unstable cycling efficiencies. The use of a 1:1 vol% mixture of DME and DGDE allowed the Li|Cu cells to cycle at this faster current density while maintaining high cycling efficiencies.

Average cycling efficiencies for the 4M LiFSI (~98%) were slightly higher than the $LiNO_3$ electrolyte utilizing dual solvents (~96%) at faster charge rates.

The ether oxygens found in short and long-chained glymes make these solvents exceptional at disassociating the $LiNO_3$ salt.[38] However, $LiNO_3$ is capable of being highly associated into aggregate solvate-Li^+ structures.[39] Additionally, these interactions increase with increasing $LiNO_3$ salt concentrations. This behavior affects the ionic mobility of lithium ions and thus electrolytes utilizing high concentrations of $LiNO_3$ electrolytes cannot be charged at high current densities. This is shown in Zhang's work; his group was able to cycle 4M LiFSI in DME up to 10 mA cm^{-2} in symmetrical Li|Li cells but were only able to cycle Li|Cu cells up to 0.6 mA cm^{-2} when a 3M $LiNO_3$ with 0.5M LiTFSI in DGDE electrolyte was utilized.[24,25] By reducing the concentration of the $LiNO_3$ salt to 1M, adding a 1M LiFSI co-salt, and utilizing a dual DME-DGDE (1:1 vol%) solvent system we were able to deposit lithium with high cycling efficiencies up to 1 mA cm^{-2}.

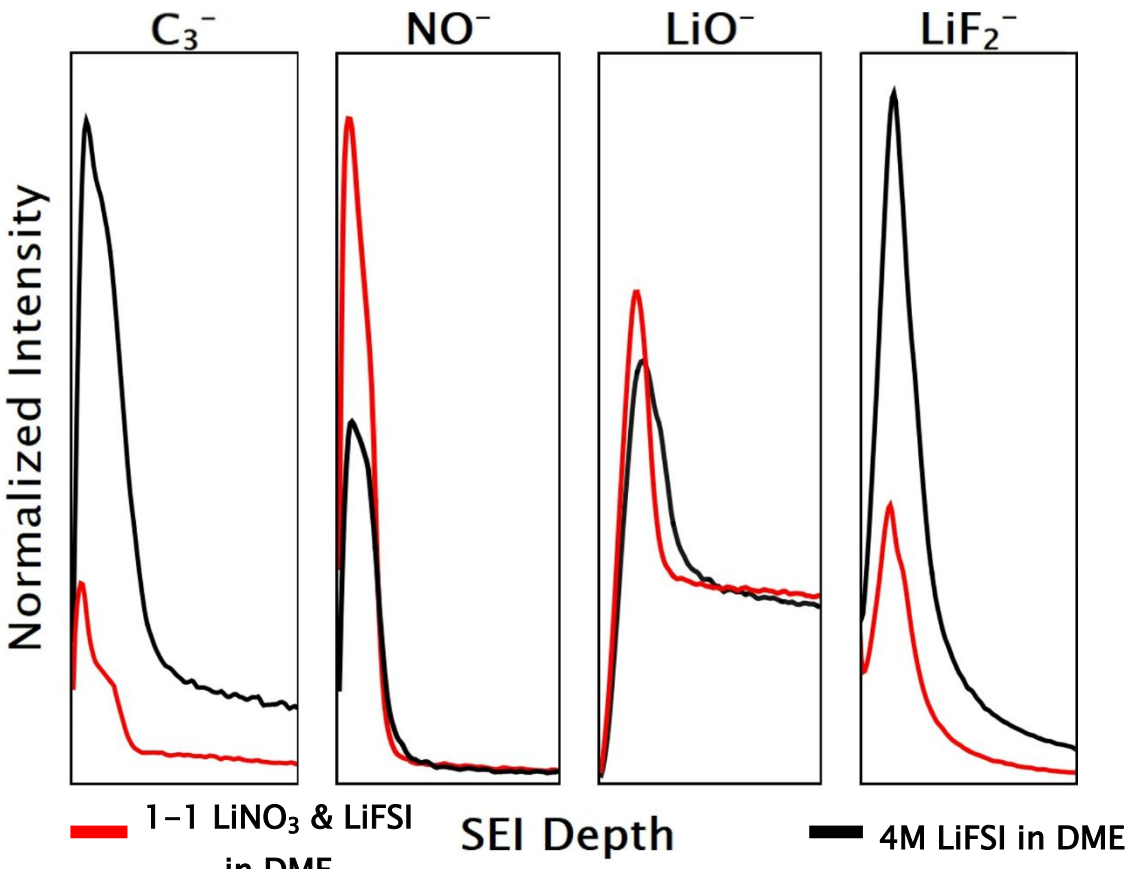

Figure 5. Time-of-flight depth profiling of the SEI formed from 4M LiFSI in DME (black)

Figure 5 shows ToF-SIMS depth profiling of the nascent lithium SEI formed in the 4M LiFSI in DME and 1M $LiNO_3$ with 1M LiFSI in DME electrolytes prior to passing charge. All the curves in this figure are normalized to the bulk Li mass (Li_3^-) and have the same x-axis range (0 to 60 seconds sputtering time). Four ionic species of interest were chosen based on the potential salt/solvent decomposition products: C_3^- was the proxy for organics such as lithium alkoxides/polyolefins; NO^- for the Li_xNO_y which forms from N-containing compounds; LiO^- was chosen for the Li_2O; and LiF_2^- denoted the LiF formed from the fluorinated anions.[25,40–42] The differences in the SEIs of the $LiNO_3$-based electrolytes formed in the DGDE:DME (1:1 vol%) and

DME (single solvent) are shown in **Figure S9**. Use of either solvent system did not significantly affect the measured species of interest.

ToF-SIMS depth profiling revealed that the inorganic components of the SEI, represented by the LiO^-, NO^-, and LiF_2^- curves, varied significantly between the 4M LiFSI and the $LiNO_3$ electrolyte. The LiF_2^- signal from the 4M LiFSI in DME electrolyte showed higher concentrations of LiF present in the SEI compared to the $LiNO_3$ electrolyte. This is likely due to the 3M concentration difference in the LiFSI salt content. The higher levels of NO^- in the $LiNO_3$ electrolyte compared to the 4M LiFSI in DME electrolyte are caused by the decomposition of the NO_3^- anion.[42] Both the electrolytes exhibited similar Li_2O decomposition layers, however the polymer organic layer (C_3^-) appeared to be greatly diminished with the $LiNO_3$ electrolyte.

The most striking result from the ToF-SIMS depth profiling is the large difference in organics found in the SEI (C_3^-). Despite having a much higher overall salt concentration, which should minimize the amount of solvent readily available to react with lithium,[24] the 4M LiFSI in DME electrolyte created a more organic rich SEI than the $LiNO_3$ electrolyte.[43,44] The presence of a dense organic decomposition layer in the SEI is unfavorable as these polymer layers tend to be porous.[45,46] The higher levels of organics formed in the 4M LiFSI electrolyte could have induced a sufficiently heterogenous lithium-ion flux through the SEI which resulted in dendrite formation. On the other hand, the concentrated $LiNO_3$ electrolyte formed an SEI with reduced organic decomposition products, which may have resulted in a smoother lithium-ion flux yielding uniform lithium electrodeposits.

Inorganics in the SEI such as Li_2O, LiF, and Li_xNO_y are favorable over polymeric species due to their higher mechanical modulus, lower solubilities in organic solvents, and superior electrical insulating properties.[6,47] LiF formation in the SEI is especially desirable due to its wide electrochemical stability window and minimal solubility in organic solvents.[48] Lithium anodes with LiF enriched SEIs have been shown to improve lithium turnover through many charge/discharge cycles and improve deposition morphology.[22,23] However, our results show that a purely LiF enriched SEI alone is not required to form an organic polymer depleted SEI that renders uniform electrodeposits.

CONCLUSIONS

In conclusion, depositions in the visualization cell demonstrated that a minimum of 1M $LiNO_3$ was sufficient in completely inhibiting three-dimensional lithium growth in linear ether electrolytes. A resurgence in non-uniform lithium deposits when the $LiNO_3$ electrolyte was cycled in coin cells was found to be caused by the porous polymer separator. These polymer separators restricted the lithium-ion flux to the electrode-contacting separator pores where the true current density was higher than the galvanostatically applied current density. Substitution of the separator by a plastic washer yielded smooth electrodeposits. These results suggest that the use of a dedicated visualization cell, where lithium electrodepositions are unencumbered by a polymer separator, may be necessary in identifying electrolytes that can truly plate uniform, dendrite-free deposits. Addition of a 1M LiFSI co-salt to the 1M $LiNO_3$ in linear ether solvents resulted in high lithium plating capacity retention in both the anode-free LFP|Cu and Li|Cu coin cell testing. Finally, ToF-

SIMS depth profiling revealed that the $LiNO_3$ based electrolytes formed a more inorganic rich SEI with markedly lower organic content than the 4M LiFSI in DME electrolyte. The results of this work show that both high cycling efficiencies and uniform lithium depositions are attainable when a 1M $LiNO_3$ concentration is used in linear ether electrolytes.

EXPERIMENTAL SECTION

Sample Preparation

Lithium of 1.5 mm thickness (Alfa 99.9%) was used for optical cell electrodepositions. The 0.75 mm thickness Li (Alfa 99.9%) was used for the Li|Cu coin cell experiments. The two electrolyte salts were $LiNO_3$ (ACROS 99%) and LiFSI (Oakwood Chemical). The two solvents used were DME (Sigma 99.5%) and diglyme (Sigma 99.5%). Before mixing the salts into the solvents, the salts were dried in vacuum at 80 °C for over 24 hours before use. Single-side coated LFP electrodes were purchased from MTI (83 μm thickness and approximately 11 mg cm^{-2} active material). Excluding the optical imaging, all electrochemical tests were performed in CR2032 coin cells. Celgard 2400 polypropylene membranes were used as separators. Coin cells were assembled in an MBRAUN, argon-filled glovebox with water and oxygen levels < 0.1 ppm.

Electrochemical Measurements

All coin cell cycling tests were carried out with an Arbin BT-2143 multichannel battery testing system. The LFP|Cu cells were allowed to rest 12 hours before cycling between 3 and 3.8 V at 0.2 mA cm^{-2} (C-Rate ~ 0.1). OCVs of LFP|Cu cells were a couple of hundred millivolts before lithium was first plated. Li|Cu cells were also rested for 12 hours prior to cycling at a constant current density of 0.5 and 1.0 mA cm^{-2}. A 1-volt upper limit was set on the stripping cycles in the

Li|Cu cells. Cu electrode diameters were 1/2" while the Li and LFP electrodes were 7/16." Care was taken to ensure LFP and lithium electrodes were completely eclipsed by the copper electrodes. All coin cells were flooded with electrolyte. Electrochemical impedance spectroscopy on the Li|Li cells were performed with a Gamry Interface 1010E potentiostat with a 0.1 – 200,000 Hz frequency range and 10 mV amplitude.

Material Characterization

The TOF.SIMS 5 by ION-TOF GmbH, 2010 was used to depth profile the SEI formed on the lithium metal. For the uncharged electrodes in **Figure 5**, the lithium samples were soaked in their electrolyte for 12 hours inside scintillation vials. Afterwards, they were rinsed with the solvent systems used in their electrolytes. Samples were kept under inert conditions utilizing a pressure-to-vacuum transfer vessel designed by the Texas Materials Institute of The University of Texas at Austin.[1] A Cs^+ beam (~80 nA, 500eV) was used to sputter a 300 x 300 μm area; Cs was chosen to decrease the work function of our material in order to increase negative ion counts. A Bi^+ analysis beam (0.4 pA, 30 keV) was rastered over a 100 x 100 μm area centered inside the Cs sputtered area, segmented into 256 x 256 pixels in high current mode. Non-interlaced mode (sputtering and surface analysis done separately) was used in all depth profiling.

Imaging

The high-resolution, optical images were taken with a Keyence VHX-5000 digital microscope. The VH-250R lens was utilized for all imaging at 250 and 500 x-magnification. The depositions in **Figure 1** and **Figure S2** were run at 0.5 mA cm^{-2} and 1 mA cm^{-2}, respectively, until 6 mAh cm^{-2} of charge was passed. The visualization cell was assembled in the aforementioned glovebox and was hermetically sealed before being brought out for imaging. Compression of the

lithium surfaces in the electrodes shown in **Figure 2c** and **Figure 2f** was prevented by replacing the Celgard separator with a polyethylene washer (~2mm thickness). The washer was filled with electrolyte and sandwiched in between two lithium electrodes prior to cycling. The Gamry Interface 1010E unit was used for the electrochemistry in the visualization cell. SEM images were taken using the FEI Quanta 650 SEM.

ASSOCIATED CONTENT

Supporting Information

Additional optical/SEM imaging, impedance measurements, coin cell cycling, and SIMS depth profiling can be found in the supporting information.

AUTHOR INFORMATION

Corresponding Author

*E-mail: mullins@che.utexas.edu.

Notes

The authors declare no competing financial interest.

ACKNOWLEDGMENT

The authors acknowledge the generous support provided by Shell, the Welch Foundation (via grants F-1131 (AH) and F-1436 (CBM)) and the National Science Foundation (CBET-1603491 (CBM)). The authors also thank Celgard Corp. for their provision of separators and Solvay Fluor

for their donation of fluoroethylene carbonate. We would also like to thank Dr. Krishnaswamy Ravi-Chandar for use of his Keyence VHX-5000 digital microscope.

REFERENCES

1 P. Albertus, S. Babinec, S. Litzelman and A. Newman, *Nat. Energy*, 2018, **3**, 16–21.
2 L. Gireaud, S. Grugeon, S. Laruelle, B. Yrieix and J.-M. Tarascon, *Electrochem. Commun.*, 2006, **8**, 1639–1649.
3 S. S. Zhang, *ACS Appl. Energy Mater.*, 2018, **1**, 910–920.
4 J. Steiger, D. Kramer and R. Mönig, *Electrochimica Acta*, 2014, **136**, 529–536.
5 R. Rodriguez, K. E. Loeffler, R. A. Edison, R. M. Stephens, A. Dolocan, A. Heller and C. B. Mullins, *ACS Appl. Energy Mater.*, 2018, **1**, 5830–5835.
6 C. Zhang, Q. Lan, Y. Liu, J. Wu, H. Shao, H. Zhan and Y. Yang, *Electrochimica Acta*, 2019, **306**, 407–419.
7 F. Qiu, X. Li, H. Deng, D. Wang, X. Mu, P. He and H. Zhou, *Adv. Energy Mater.*, **0**, 1803372.
8 S. Xiong, Y. Diao, X. Hong, Y. Chen and K. Xie, *J. Electroanal. Chem.*, 2014, **719**, 122–126.
9 M. Wang, L. Huai, G. Hu, S. Yang, F. Ren, S. Wang, Z. Zhang, Z. Chen, Z. Peng, C. Shen and D. Wang, *J. Phys. Chem. C*, **122**, 9825–9834.
10 M. L. Meyerson, J. Sheavly, A. Dolocan, M. Griffin, A. Pandit, R. Rodriguez, R. M. Stephens, D. V. Bout, A. Heller and C. Mullins, *J. Mater. Chem. A*, **7**, 14882–14894.
11 S. Li, M. Jiang, Y. Xie, H. Xu, J. Jia and J. Li, *Adv. Mater.*, 2018, **30**, 1706375.
12 C. Peabody and C. B. Arnold, *J. Power Sources*, 2011, **196**, 8147–8153.
13 P. Bai, J. Li, F. R. Brushett and M. Z. Bazant, *Energy Env. Sci*, **9**, 3221–3229.
14 C.-Z. Zhao, P.-Y. Chen, R. Zhang, X. Chen, B.-Q. Li, X.-Q. Zhang, X.-B. Cheng and Q. Zhang, *Sci. Adv.*, 2018, **4**, eaat3446.
15 X.-B. Cheng, T.-Z. Hou, R. Zhang, H.-J. Peng, C.-Z. Zhao, J.-Q. Huang and Q. Zhang, *Adv. Mater.*, 2016, **28**, 2888–2895.
16 C.-H. Chang, S.-H. Chung and A. Manthiram, *Adv. Sustain. Syst.*, 2017, **1**, 1600034.
17 P. Barai, K. Higa and V. Srinivasan, *J. Electrochem. Soc.*, 2018, **165**, A2654–A2666.
18 H. J. Chang, N. M. Trease, A. J. Ilott, D. Zeng, L.-S. Du, A. Jerschow and C. P. Grey, *J. Phys. Chem. C*, 2015, **119**, 16443–16451.
19 M. Genovese, A. J. Louli, R. Weber, S. Hames and J. R. Dahn, *J. Electrochem. Soc.*, 2018, **165**, A3321–A3325.
20 A. J. Louli, M. Genovese, R. Weber, S. G. Hames, E. R. Logan and J. R. Dahn, *J. Electrochem. Soc.*, 2019, **166**, A1291–A1299.
21 D. P. Wilkinson, H. Blom, K. Brandt and D. Wainwright, *J. Power Sources*, 1991, **36**, 517–527.
22 E. Markevich, G. Salitra, F. Chesneau, M. Schmidt and D. Aurbach, *ACS Energy Lett.*, **2**, 1321–1326.
23 X.-Q. Zhang, X.-B. Cheng, X. Chen, C. Yan and Q. Zhang, *Adv. Funct. Mater.*, 2017, **27**, 1605989.
24 J. Qian, W. A. Henderson, W. Xu, P. Bhattacharya, M. Engelhard, O. Borodin and J.-G. Zhang, *Nat. Commun.*, 2015, **6**, 6362.
25 B. D. Adams, E. V. Carino, J. G. Connell, K. S. Han, R. Cao, J. Chen, J. Zheng, Q. Li, K. T. Mueller, W. A. Henderson and J.-G. Zhang, *Nano Energy*, 2017, **40**, 607–617.
26 S. S. Zhang, *Electrochimica Acta*, 2012, **70**, 344–348.
27 X. Liang, Z. Wen, Y. Liu, M. Wu, J. Jin, H. Zhang and X. Wu, *J. Power Sources*, 2011, **196**, 9839–9843.
28 Y. Liu, D. Lin, Y. Li, G. Chen, A. Pei, O. Nix, Y. Li and Y. Cui, *Nat. Commun.*, 2018, **9**, 3656.
29 A. Pei, G. Zheng, F. Shi, Y. Li and Y. Cui, *Nano Lett.*, **17**, 1132–1139.
30 K. N. Wood, E. Kazyak, A. F. Chadwick, K.-H. Chen, J.-G. Zhang, K. Thornton and N. P. Dasgupta, *ACS Cent. Sci.*, **2**, 790-801.

31 W. Li, H. Yao, K. Yan, G. Zheng, Z. Liang, Y.-M. Chiang and Y. Cui, *Nat. Commun.*, 2015, **6**, 7436.
32 P. Bai, J. Guo, M. Wang, A. Kushima, L. Su, J. Li, F. R. Brushett and M. Z. Bazant, *Joule*, 2018, **2**, 2434–2449.
33 M. D. Tikekar, L. A. Archer and D. L. Koch, *Sci. Adv.*, **2**, e1600320.
34 E. Khoo, H. Zhao and M. Z. Bazant, *J. Electrochem. Soc.*, 2019, **166**, A2280–A2299.
35 J.-H. Han, E. Khoo, P. Bai and M. Z. Bazant, *Sci. Rep.*, 2014, **4**, 1–8.
36 J.-H. Han, M. Wang, P. Bai, F. R. Brushett and M. Z. Bazant, *Sci. Rep.*, 2016, **6**, 1–12.
37 T. Hirai, I. Yoshimatsu and J. Yamaki, *J. Electrochem. Soc.*, 1994, **141**, 611–614.
38 W. A. Henderson, *J. Phys. Chem. B*, 2006, **110**, 13177–13183.
39 W. A. Henderson, N. R. Brooks and W. H. Smyrl, *Acta Crystallogr. Sect. E Struct. Rep. Online*, 2002, **58**, m500–m501.
40 G. G. Eshetu, T. Diemant, S. Grugeon, R. J. Behm, S. Laruelle, M. Armand and S. Passerini, *ACS Appl. Mater. Interfaces*, 2016, **8**, 16087–16100.
41 K. Leung, F. Soto, K. Hankins, P. B. Balbuena and K. L. Harrison, *J. Phys. Chem. C*, 2016, **120**, 6302–6313.
42 S. Xiong, K. Xie, Y. Diao and X. Hong, *Electrochimica Acta*, 2012, **83**, 78–86.
43 K. Tasaki, A. Goldberg, J.-J. Lian, M. Walker, A. Timmons and S. J. Harris, *J. Electrochem. Soc.*, 2009, **156**, A1019–A1027.
44 R. L. Sacci, J. M. Black, N. Balke, N. J. Dudney, K. L. More and R. R. Unocic, *Nano Lett.*, 2015, **15**, 2011–2018.
45 D. Aurbach, *J. Power Sources*, 2000, **89**, 206–218.
46 S. Shi, P. Lu, Z. Liu, Y. Qi, L. G. Hector, H. Li and S. J. Harris, *J. Am. Chem. Soc.*, 2012, **134**, 15476–15487.
47 X.-B. Cheng, R. Zhang, C.-Z. Zhao, F. Wei, J.-G. Zhang and Q. Zhang, *Adv. Sci.*, 2016, **3**, UNSP 1500213.
48 J. Ko and Y. S. Yoon, *Ceram. Int.*, **45**, 30–49.